EFDA–JET–PR(12)44

G. Arnoux, T. Farley, C. Silva, S. Devaux, M. Firdaouss, D. Frigione, R. Goldston,
J. Gunn, J. Horacek, S. Jachmich, P.J. Lomas, S. Marsen, G.F. Matthews,
R.A. Pitts, M. Stamp, P. Stangeby and JET EFDA contributors

Scrape-Off Layer Properties of ITER-Like Limiter Start-Up Plasmas in JET

Scrape-Off Layer Properties of ITER-Like Limiter Start-Up Plasmas in JET

G. Arnoux[1], T. Farley[2], C. Silva[3], S. Devaux[4], M. Firdaouss[5], D. Frigione[6], R. Goldston[7], J. Gunn[5], J. Horacek[8], S. Jachmich[9], P.J. Lomas[1], S. Marsen[10], G.F. Matthews[1], R.A. Pitts[11], M. Stamp[1], P. Stangeby[12]
and JET EFDA contributors*

JET-EFDA, Culham Science Centre, OX14 3DB, Abingdon, UK

[1]*EURATOM-CCFE Fusion Association, Culham Science Centre, OX14 3DB, Abingdon, OXON, UK*
[2]*ITER organisation, Fusion Science and Technology Department, Cadarache, 13108 St Paul-Lez-Durance, France.*
[3]*Associao EURATOM/IST, Instituto de Plasmas e Fuso Nuclear, Instituto Superior Tcnico, Av Rovisco Pais, 1049-001 Lisbon, Portugal*
[4]*Max-Planck-Institut fr Plasmaphysik, EURATOM-Assoziation, 85748 Garching, Germany*
[5]*Association EURATOM-CEA, CEA/DSM/IRFM, Cadarache 13108 Saint Paul Lez Durance, France*
[6]*Associazione EURATOM-ENEA sulla fusione, C.R Frascati, Roma, Italy*
[7]*Princeton Plasma Physics Laboratory, Princeton, NJ 08543, USA*
[8]*Association EURATOM-IPP.CR, Institute of Plasma Physics AS CR, Za Slovankou 3, 182 21 Praha 8, Czech Republic*
[9]*Association "EURATOM - Belgian State" Laboratory for Plasma Physics Koninklijke Militaire School - Ecole Royale Militaire Renaissancelaan 30 Avenue de la Renaissance B-1000 Brussels Belgium*
[10]*Max-Planck-Institut fr Plasmaphysik, Teilinstitut Greifswald, EURATOM Assoziation, 17491 Greifswald, Gemany*
[11]*ITER Organization, Route de Vinon sur Verdon, 13115 Saint Paul Lez Durance, France*
[12]*University of Toronto, Institute for Aerospace Studies, Toronto, M3H 5T6, Canada*
** See annex of F. Romanelli et al, "Overview of JET Results", (24th IAEA Fusion Energy Conference, San Diego, USA (2012)).*

Preprint of Paper to be submitted for publication in
Nuclear Fusion

ABSTRACT.
Recent experiments at JET combining reciprocating probe measurements (upstream) and infrared thermography (at the plasma facing components (PFC)) on plasmas in limiter configurations show that the common approach to predicting the power load on the limiter underestimates the heat flux at the contact point by a factor 1.5–3. The current model and scaling laws used for predicting the power load onto the first wall during limiter current ramp-up/down in ITER are uncertain and a better understanding of the heat transport to the PFCs is required. The heat loads on PFCs are usually predicted by projecting the parallel heat flux associated with scrape-off layer (SOL) properties at the outer mid-plane (upstream) along the magnetic field lines to the limiter surface and deducing the surface heat flux through a cosine law, thus ignoring any local effect of the PFC on transport within the SOL. The underestimate of the heat flux is systematic in inner wall limiter configurations, independent of the plasma parameters, whereas in outer limiter configuration this is not observed, probably because of the much shorter SOL power decay length. Models that can explain this enhanced heat flux around the contact point are proposed and discussed but at this stage one cannot give a final conclusion.

1. INTRODUCTION

The plasma power load onto the first wall plasma facing components (PFC) during the current ramp-up/down in ITER must be minimised in order to avoid possible melting of the beryllium tiles which armour the actively cooled first wall [1]. The commonly employed technique to predict power loads onto the PFCs, q_{lim}, is to start from an assumed scrape-off layer (SOL) heat flux profile, $q_{||}(r_{mid})$, at the outer mid-plane (omp), where rmid is the radial distance from the omp last closed flux surface (LCFS), and project these properties along the magnetic field lines, **B**, to the PFCs such that:

$$q_{lim} = (R_{omp} / R_{lim}) \cdot cos(\theta_n) \cdot q_{||} \tag{1}$$

with $\cos(\theta_n) = \hat{n} \bullet \mathbf{B}/_{||}\mathbf{B}_{||}\ \hat{n}$ and n is the normal vector to the PFC surface. The ratio $R_{omp} = R_{lim}$ accounts for the flux expansion with R_{omp} the radial position of the LCFS at the omp and R_{lim} the radial position of the plasma contact point on the limiter. The heat flux profile is further assumed to be exponential such that:

$$q_{||}(r_{mid}) = q_{0||} \cdot e^{-r_{mid}/\lambda_{q,omp}} \tag{2}$$

where $q_{0||}$ is the heat flux at the LCFS and λ_q the power decay length. This is the method employed, for example, by the field line tracing and surface heat flux calculation code PFC Flux [2], which will be used below to compare with experimental infrared (IR) measurements.

Previous publications [3, 4] discussed the conditions when it is appropriate (and inappropriate) to project $q_{||}(r_{mid})$ along **B**, but the case of a limiter plasma was not examined there. It was observed

20 years ago that q_{lim} in the vicinity of the limiter tangency point is higher than the simple cosine law would predict [5, 6, 7] and it was attributed to the “funnel” effect proposed in [8]. However the model described only qualitatively the measurements. The new measurements in JET limiter plasmas reported here provide a new opportunity to investigate the “funnel” model (FM) on a large data set. As illustrated in the example of Figure 1 the gradient of the inferred $q_{||}$ is much steeper in the near SOL ($r_{mid} \leq 5$mm, $\lambda_{q;near} = 5.5$mm) than in the far SOL ($\lambda_{q;far} = 22$mm). This profile was derived from IR camera measurements of q_{lim} on the limiter surface and projected back to the outer mid-plane using Equation (1). Independent measurements in the SOL upstream of the limiter using a fast reciprocating Langmuir Probe (RCP), indicate that upstream profiles do follow an exponential decay (see Figure 2), although the region of $r_{mid} < 5$mm could not be accessed by the probe in the experiments here. Furthermore, this effect is observed only in IWL configurations. The question is then: is the enhanced heat flux observed in the near SOL due to a local action of the limiter which is not captured in the free SOL? And does the FM explain these measurements? It is essential to answer these questions and understand the physics behind it if one wants to be able to make accurate predictions of the power loads to the first wall in ITER.

The present scaling used for ITER is based on L-mode diverted plasmas [9] and usesonly RCP data. There is no credit given to any enhanced heat flux effect on the limiter surface which has been observed in the new JET data. Recent RCP measurements on Tore Supra (TS), over a large range of plasma current, I_p, plasma density, n_e, and edge safety factor, q_{edge}, have shown that the present ITER scaling is unsatisfactory [10]. A new multi-machine scaling must be found for limiter configurations and is in the process of being compiled and analysed under the auspices of the International Tokamak Physics Activity (ITPA) Divertor and SOL physics Topical Group. In this contribution we discuss the JET database in the context of the inverse ohmic power law found with the TS data.

2. MEASUREMENTS AND METHODS

2.1. EXPERIMENTS

In order to contribute to a multi-machine scaling for q, a dedicated scenario, optimised for the edge diagnostics, was repeated (for a total of 35 JET pulses) scanning the key operational parameters: the plasma current, $1.2 < I_p < 2.5$MA, the plasmas density (line integrated), $3.8 < n_{e,l} < 8.0 \cdot 10^{19}$ m^{-2}, and the heating power, $0.7 < P_{heat} < 4.4$MW. The magnetic field was fixed, $B_\phi = 2.7$T, yielding a scan in q_{edge} through the I_p variation ($2.7 < q_{edge} < 6.9$).

An illustration of the typical scenario and magnetic configurations are shown in Figure 3. The scenario for ohmic discharges (26 out of the 35 cases studied here) is divided into two phases. The scenario starts with an inner wall limiter (IWL) configuration that lasts for about 16s, with current and density plateau for about 10s (50s < t < 60s). During that first phase the IR measurements are optimal since the energy deposited onto the limiter is maximised. During that first phase, one measurement with the RCP is taken at 52s (the reciprocation takes 0.5s to complete its cycle). The transition to the second phase occurs at $t = 6s$, when the plasma is moved outward to an outer wall limiter (OWL) configuration. The transition can be identified by the change of radial inner (RIG) and outer (ROG) gap between the LCFS and the limiter at $z = 0$ and by the short dip in the plasma current. Note that $z = 0$ is about 30cm below the plasma omp for these limiter configurations. One notes that the density systematically increases in OWL configuration. In the second phase, a second measurement with the RCP is taken.

The different operational constraints on the two key diagnostics (IR and RCP) did not allow complete coverage of the same parameter range. For the probe to reciprocate close enough to the LCFS, the operational procedure requires to repeat exactly the same plasma scenario up to 4 times and get step by step closer and closer to the LCFS, with sanity checks by the RCP operator between pulses. In other words, measuring SOL profiles down to the LCFS with the RCP costs 3 to 4 plasma pulses per configuration/scenario. On the other hand, one can get a measurements in IWL and OWL configuration in a single pulse, allowing for direct comparisons between IWL and OWL configurations. Because the IR camera is a passive diagnostic, good measurements can be taken over a wider range of I_p, $n_{e,l}$ and P_{heat} (1 pulse = 1 good measurement). On the other hand, to collect good data requires a long pulse in order to maximise the energy deposited onto the limiter. A comparison between IWL and OWL configuration in a single pulse is therefore not feasible. In this paper most of the IR data has been in IWL configuration (30 out of 35 pulses).

2.2. DETERMINATION OF THE INFERRED QK(RMID) WITH RCP MEASUREMENTS

The Langmuir probe measures the ion saturation current, I_{sat} and the electron temperature, T_e, derived from the current-voltage characteristic of the probe (Figure 2 (b) and (c)). For sheath-limited conditions at the probe, and if $T_e = T_i$, $q_{||}(r_{mid}) = \gamma_{||}\Gamma_{||}(r_{mid})T_e(r_{mid})$ where $\gamma_{||}$ is the parallel sheath transmission factor and $\Gamma_{||} = I_{sat}/e$ with e the electron charge. The power decay length can be either deduced from the temperature decay length, T_e and the ion saturation current decay length, I_{sat} such that: $1/\lambda_q = 1/\lambda_{Te} + 1/\lambda I_{sat}$ or by fitting equation (2) to $q_{||}(r_{mid})$. The first method requires no knowledge of the absolute value of the heat flux. In the second case, $q_{||}(r_{mid})$ is usually estimated assuming a fixed value of $\gamma_{||}$ ($\gamma_{||} = 8$ here). More details of the RCP data can be found in [11].

The JET probe head is equipped with different pins (Figure 4) and the resulting I_{sat} and T_e can depend on the analysis method, and to a lower extent, on which pin is used. In this contribution, two sets of independently analysed data will be used (labelled RCP I and RCP II), leading to slightly different results. The main difference in the results is attributed to the method used to fit the voltage current characteristic of the swept probe (labelled n – e, T_e in Figure 4(b))

2.3. DETERMINATION OF THE INFERRED $q_{||}(r_{mid})$ WITH IR MEASUREMENTS

The wide angle view IR system at JET [12] can measure the surface temperature, $T_{lim}(x, y, t)$, of the inner wall guard limiter (IWGL), module 8Z and of the wide outer poloidal limiter (WOPL), module 1D, both made of highly shaped, castellated, beryllium tiles [13]. The heat load associated with each pixel (x, y), $q_{lim}(x, y, t)$, is derived from $T_{lim}(x, y, t)$ using the non-linear finite difference code THEODOR [14]. In the specific case of the JET limiters, because of the tile castellation (12×12mm) lateral diffusion (parallel to the PFC surface) can be neglected and the heat diffusion equation is resolved only into the depth of the tile. Note that the pixel resolution (15–20mm) is of the same order as that of the castellation size. In our analysis $q_{lim}(x, y, t)$ is time averaged over a window of 500ms: $\langle q_{lim}(x, y, t)\rangle t = q_{lim}(x, y)$.

To relate qlim(x; y) to the topology of a given magnetic equilibrium, the IR image of the limiter (see example in Figure 5(a)) is mapped in 3D geometry to obtain a 2D surface in cylindrical co-ordinates: $\{R(x, y); z(x, y); \phi(x, y)\}$, with R the radial position, z the vertical position and the toroidal position of the surface of the object seen by each pixel. A heat flux map can then be constructed, for example in the ϕ–z plane as illustrated in Figure 5(b). For a given magnetic equilibrium, the heat flux map $q_{lim}(\phi, z)$ can be directly associated with an omp map, $r_{mid}(\phi, z)$ (Figure 5(c)) and a field line angle map, $\theta_n(\phi, z)$ (Figure 5(d)). Using the three maps: $q_{lim}(\phi, z)$, $r_{mid}(\phi, z)$ and $n(\phi, z)$ with Equation (1) and Equation (2) yifields the inferred $q_{||}(r_{mid})$ profile as illustrated in the examples of Figure 1. From a least-square fit, λ_q can then be derived. In this process, it is important to carefully select the pixels in $q_{lim}(\phi, z)$ (see mask in Figure 5(e)). For the analysis here, we used three selection criteria:

(i) The pixel must be in a wetted area (it must be connected to the omp). The flux map predicted by PFC Flux in Figure 5(f) shows the shadowed area (in grey). If one uses pixels in the shadowed area, the inferred profile splits into two branches with two different slopes. These two slopes can be understood by looking at the poloidal cuts of q_{lim} in Figure 6(c). The poloidal cut on the electron-drift side, at $\phi = 1.04$ rads, shows a positive slope in the range $-0.6 < z < 0.33$m ($z = 0.33$ m is the plasma contact point). This slope is the result of the power decay in the SOL. Past the plasma contact point, a much steeper, negative slope is observed. This is representative of the transition from the wetted to the shadowed area. If one looks at the ion-drift side ($\phi = 1.09$ rads), the same typical profile is observed but upside down. At the limiter ridge, at $\phi = 1.06$, one does not see the steeper slope because the ridge is always wetted, either from the ion or from the electron drift side.

(ii) The pixel must have $q_{lim} > 0$, in other words, it must have a significant heat load and not be affected by re-deposited layers, which are known to have poor thermal contact with the bulk of the tile.

(iii) For the IWGL, the pixel must be located on the electron drift side (left hand side) of the limiter. This is imposed as a consequence of some ambiguities in the interpretation of the IR image on the ion drift side - the high heat flux area slightly above the contact point on the right hand side is not completely understood, but is thought to be related to an embedded Langmuir probe.

Figure 1 shows the inferred $q_{||}(r_{mid})$ from the IR measurement for an IWL (a) and an OWL (b) configuration, and for comparable plasma parameters: $P_{SOL} \simeq 3.5$MW, $n_{e,l} = 6.9 \cdot 10^{19}$ m^{-2}, $I_p =$ 2.0MA and B = 2.7T ($q_{edge} \simeq 3.5$). Two main conclusions can be drawn from these examples, which are representative of the whole database:

(i) The inferred parallel heat flux profile on the IWL is not a single exponential and has a much steeper gradient in the near SOL (r_{mid} < 5mm). The profile can be characterised by two exponential functions with different decay lengths: $\lambda_{q,far}$ (= 20mm in this example) and $\lambda_{q,near}$ (= 5.5 mm in this example) for the far and near SOL respectively, such that

$$q_{\|}(r_{mid}) = \begin{cases} q_{0\|,near}\, e^{-r_{mid}/\lambda_{q,near}} & if \quad r_{mid} \le r_{break} \\ q_{0\|,far}\, e^{-r_{mid}/\lambda_{q,far}} & if \quad r_{mid} \ge r_{break} \end{cases} \tag{3}$$

where rbreak is the rmid value where the break in the slope occurs.

(ii) The parallel heat flux profile in the OWL is exponential (at least no clear break in the slope is observed) and the power decay length is much smaller (q ~ 8mm) than that of the IWL far SOL.

2.4. COMPARISON BETWEEN IR AND RCP MEASUREMENTS

Figure 7(a) shows the power decay length deduced from the RCP measurements using method II as a function of that using method I. It shows that despite a large apparent scatter, both method agree within error bars.

Figure 7(b) shows the power decay length measured by the IR in the far SOL, $\lambda_{q,far,IR}^{IWL}$ as a function of that measured by the RCP, $\lambda_{q,RCP}^{IWL}$ for the IWL configurations only. One distinguishes two clouds of data. The higher values of $\lambda_{q,IR,far}^{IWL}$ (> 60 mm) all correspond to plasmas with I_p < 1.7MA. One finds that $\lambda_{q,IR,far}^{IWL} > \lambda_{q,RCP}^{IWL}$ by up to a factor 4.5. On the other hand for higher plasma currents (I_p > 1.7MA), $\lambda_{q,IR,far}^{IWL} < \lambda_{q,RCP}^{IWL}$ down to a factor 2.5 for the worst case. A significant amount of the data point are not in agreement within the error bars.

It is not clear why this discrepancy is observed and why there is a separation between high and low current plasmas (and why at I_p = 1.7MA). Except the method and the instruments, the main difference between the two diagnostics is the extent of the SOL covered by the measurements. While the RCP measures in the SOL almost from the LCFS to r_{mid} ~ 120mm, which corresponds to 2–3 power decay length, the IR only measures from the LCFS to r_{mid} ~ 30–40mm, which corresponds to 0.5–1.0 power decay length. The fit on the IR data can therefore lead to inaccurate estimate of q, which explains the scatter in Figure 7 but does not explain the split into two clouds. It can also indicate that the profiles are not perfectly exponential and that the value of q depends on what part of the profile one uses to fit the data.

2.5. VALIDATION OF THE MEASUREMENTS WITH A POWER BALANCE

A common method used to validate heat flux measurements is to perform a power balance. The power entering the SOL can be derived from the following formula [15]:

$$P_{SOL,meas} = 2\pi R_{LCFS} \frac{B_\theta}{B_\varphi} \cdot \int_0^{r_{wall}} 2q_{||}(r_{mid})dr_{mid} = 4\pi \frac{B_\theta}{B_\varphi} \lambda_q q_{0||} \tag{4}$$

where B_θ is the poloidal components of the total magnetic field and the B–field components are evaluated at R_{LCFS}. The second equality comes from using Equation (4) and taking $r_{wall} = \infty$ but this is not applied to the IR IWL data because the profiles are not single exponential. Instead, the integral is evaluated using the two exponential functions such that:

$$P_{SOL,IR} = 4\pi R_{LCFS} \frac{B_\theta}{B_\varphi} \cdot \left[\left(1 - e^{-r_{break}/\lambda_{q,near}}\right) \lambda_{q,near}\, q_{0||,near} + \lambda_{q,far}\, q_{0||,far} \cdot e^{-r_{break}/\lambda_{q,far}} \right] \tag{5}$$

where $q_{0||,far}$ is the value of $q_{||}$ at the LCFS back extrapolated from the far SOL fit function and r_{break} indicate the breakpoint between the near and the far SOL. In our experiments, r_{break} = 5–6 mm for the whole database. The power to the SOL can also be deduced from power balance:

$$P_{SOL,bal} = P_{heat} - P_{rad} - dW_{th}/dt \tag{6}$$

where P_{rad} is the power radiated into the core plasma (measured with bolometers) and dW_{th}/dt is the change in the energy confinement.

Figure 8(a) shows $P_{SOL,meas}$ deduced from Equation (4) and Equation (5) as a function of PSOL;bal, deduced from Equation (6) for the RCP and IR measurements respectively. The RCP measurements give a reasonable power balance within 70 and 110% for most of the data points (and two extreme data points at 138% and 53%). There is a strong difference in the IR data set between IWL and OWL plasmas. The latter provide good power balance (~ 90%), but for the IWL, whilst agreement is reasonable at low P_{SOL} (ohmic plasmas with I_p < 1.5MA) only ~ 50% power balance is achieved at higher P_{SOL}. It is not clear where the mismatch comes from but it seems to correlate with I_p (Figure 8 (b)). One can invoke 4 possibilities, keeping in mind that one achieve good power balance for the OWL cases:

(i) The calibration of the IR diagnostic underestimates the temperature and therefore the heat flux.

(ii) There is a toroidal asymmetry of the heat load pattern on the limiter between the ion and electron drift side. Since one uses the e-drift side only for the inferred profile, one misses some power.

(iii) The power load onto the 10 IWGL is not evenly distributed (possibly due to misalignment) and the IWGL 8Z is partially in the shadow of the other limiters.

(iv) The flux expansion is not taken properly into account when the mapping to the outer mid-plane is performed.

Figure 8(b) gives us an indication of what it might be. It shows a clear correlation between the mismatch and the plasma current. Given that B_ϕ is the same for every plasma, Ip is directly correlated with the field line angle onto the limiter. The higher I_p (and B) the greater the mismatch. This dependence of $P_{SOL,IR}/P_{SOL,bal}$ on B_θ indicates that the explanation is probably a combination of (ii) and (iv). The map of qlim in Figure 5(b) suggests that the heat load is higher on the ion-drift side than it is on the e-drift side. This asymmetry can partially be explained by the uneven distribution of the limiters around the machine. The PFC Flux simulation in Figure 5 (f) shows that one would expect a higher power load on the i-drift side. At this stage the analysis of the PFCFLFlux results do not allow to investigate this further. The asymmetry i/e- drift side on one case (JET Pulse No: 80836) has been analysed and is illustrated in Figure 6. The toroidal slices of qlim for example show that $q_{lim}(z = 0.404)$ (i-drift side) has its peak value about 20% higher than for $q_{lim}(z = 0.213)$ (e-drift side). Is that enough to explain the 50% missing power? It is unlikely. Note that this asymmetry is not observed for the OWL configuration, where we use both sides of the limiter to infer $q_{||}(r_{mid})$.

There is also evidence (Be melt events) that the heat loads are not evenly shared between the 10 IWGL [16] and this may explain why the power balance is not closed (explanation (ii)). However there is no reason to think that this kind of asymmetry should occur only on the IWGL but it could also happen to the WOPL. This matter is the subject of on-going investigations. Further work will be done to understand this and we will not pursue further in this paper.

3. DISCUSSION

3.1. IWL AND OWL CONFIGURATIONS

JET results systematically show a strong asymmetry in λ_q between IWL and OWL configurations: $\lambda^{IWL}_{q,RCP}/\lambda^{OWL}_{q,RCP} = 6.2\pm0.6$ and $\lambda^{IWL}_{q,IR} / \lambda^{OWL}_{q,IR} = 2.58\pm0.01$. It has already been observed on several tokamaks that the plasma out flux is localised in a region around the omp. Experiments on TS, for example, indicate that the enhanced low field side out flux occurred over a poloidal extent of $\theta = \pm30^o$ around the omp [17]. In the JET experiments described here, the connection length (between the limiter and the omp) is much shorter for OWL: $L_c < 1.2$m (half the toroidal distance between two WOPL), than for IWL: $25 < L_c < 52$m $(2.9 < q_{edge} < 6.0)$ configurations and can explain this asymmetry in λ_q but it is not clear whether this is the only effect. Recycling and impurity (beryllium in JET) in flux also appear to be different, especially in neutral beam heated (NBI) plasmas. A maximum of $Z_{eff} = 2.6$ is found for IWL cases at the highest NBI power whereas Z_{eff} reaches 3.8 in a similar case in OWL plasmas. The level of SOL turbulence is also found to be much smaller for OWL [11], which is consistent with a shorter λ_q. The factor 2 difference found between the IR and RCP measured ratio (IWL/OWL) is mainly due to the fact that $\lambda^{IWL}_{q,far,IR} \sim (0.6\pm0.1)\lambda^{IWL}_{q,RCP}$ for $I_p > 1.7$MA (Figure 7(b)) and that $\lambda^{OWL}_{q} = 8 \pm 1$ for all the measurements, independently of the diagnostic and plasma parameters. Note that for the IR, a direct comparison was only possible for two pulses at high beam power (the two highest P_{SOL} in the database).

The other noticeable difference between IWL and OWL configuration is the shape of the inferred

$q_{||}$ profiles from the IR measurements. While there is an enhancement of qk in the near SOL of the IWL profiles (Figure 1 (a)), it is not visible on the OWL profiles (Figure 1 (b)). Our measurements indicate that the enhanced heat flux is due to the funnel effect at the limiter (see section 3.4), in which case we would expect to see it in the two configurations. And we do see an enhancement if one looks at the heat flux maps rather than at the inferred $q_{||}$ profiles. Figure 9 shows in (a) the same maps as in Figure 5 (b) and (f) for an IWL configuration (PFCFLFlux simulation and IR measurement) and in (b) similar maps but for an OWL configuration.

Let us compare first the PFCFLFlux simulation and the IR measurements at the plasma contact point for the IWL configuration. At the plasma contact point, the measurement clearly exhibit a local maximum, which is not predicted by PFCFLFlux. This is what we call the enhanced heat flux.

The OWL map also shows an enhancement at the plasma contact point. While the PFCFLFlux simulation show maxima away (but rather close) from the limiter ridges (note that they are oblique for the OWGL), the measurement clearly shows that the heat flux peaks on the ridge. Why does it not appear on the inferred profiles then? In order for the enhanced heat flux to be visible in the inferred profiles, one needs to see a clear break in the slope of $q_{||}$. Probably because λ_q (= 8mm) is too small and very close to the $\lambda_{q,design}$ ($\lambda_{q,design}$ = 10mm), we do not see it in the inferred $q_{||}$. (Note that the heat flux is supposed to be evenly distributed on the tile surface if $\lambda_q = _{q,design}$.). The fact that λ_q^{OWL} > 20mm, ie at least two time larger than q;design may explain why it is much more noticable on the IWL inferred profiles.

3.2. MULTI-MACHINE SCALING LAW FOR Q

Recent work on TS has shown that the power decay length in IWL configuration depends on the ohmic power:

$$\lambda_q = C \cdot P_\Omega^\alpha = C \cdot (P_{heat}/V_p)^\alpha \tag{7}$$

where C and α are fit coefficients [10], P_{heat} is the heating power and V_p is the plasma volume. The second equality is strictly true for the TS database since only ohmically heated plasmas have been used. Two different scaling laws have in fact been found on TS depending on the type of probe and method used. In one case, only a tunnel probe (TUN) was used and in the second case a combination of two measurements, one with the tunnel probe and the second with a retarding field analyser (TUN + RFA) was used. The result is that λ_q is almost a factor 2 lower with the (TUN+RFA) method. Table 1 shows the different fit parameters using the second expression of Equation (7). Replacing P_Ω by P_{heat}/V_p is useful when one wants to compare TS data with JET data. Figure 10 compiles q for the JET IWL plasmas (IR and RCP) and TS (RCP) databases as a function of P_{heat}/V_p. Note that for JET IR data, only $\lambda_{q,far}$ has been used in this plot. The two scaling laws found in [10] are also indicated. The IR points are in line with the scaling law derived from the RFA+TUN method (TS data not shown here) when P_{heat}/V_p > 15000kW/m^3. However, the scatter on this plot still is large and further work is undertaken to find a better scaling law.

3.3. ENHANCED DEPOSITED HEAT FLUX NEAR THE LIMITER TANGENCY POINT

The inferred parallel heat flux profiles in IWL configurations, reconstructed from the IR measurements using the cos(n) law systematically show an enhanced heat flux (see examples in Figure 1(a) and Figure 12) in the near SOL (r_{mid} < 5mm). This results from the higher heat flux measured around the plasma contact point (centre of Figure 5(b)) than would be predicted with PFCFlux (Figure 5(f)). The same effect has been observed in one example case on TS [18], but this was not systematically explored at the time. We characterise these profiles using Equation (3) and the two power decay lengths: $\lambda_{q,near}$ and $\lambda_{q,far}$. Note that using Equation (3) is not motivated by a physical interpretation of the profiles, it is only a practical way of characterising them. Figure 11(a) shows the ratio $\lambda_{q,near}/\lambda_{q,far}$ as a function of P_{SOL} for the 30 JET pulses. The different symbols (and colours) distinguish different density ranges. This figure indicate that $q_{||}$ is 10–5 times steeper in the near SOL than it is in the far SOL. We observe no dependence of this effect on P_{SOL} or on $n_{e,l}$. As shown in Figure 11(b), the inferred heat flux at the LCFS, $q_{||0,near}$, is 1.5–3 times higher than that predicted using a simple extrapolation from the far SOL profile, $q_{||0,far}$. The consequence on the limiter is that the heat load around the contact point is 1.5–3 times higher than what the cos(n) law would predict. Here again we observe no dependence on the main plasma parameters (I_p, P_{SOL}, $n_{e:l}$). Note also that for the whole database rbreak ~ 5–6mm.

The most likely explanation of the enhanced heat flux is the local sink action of the limiter, the so-called funnel effect [8]. The $q_{||}$ profiles systematically show a scatter around the fit value of typically 1MW/m^2, with a clear systematic dependence on cos(n) (see example in Figure 12). If the cos(n) law hfield true, ~~o~~ne would expect this scatter distribution to be independent of cos(n). Let us define the residual:

$$\delta q_{||} = q_{||}(r_{mid}\,, \theta_n) - \hat{q}_{||}(r_{mid}) \tag{8}$$

where $\hat{q}_{||}(r_{mid})$ is the fit function described by Equation (3) and $q_{||}(r_{mid,\,n})$ represents the data points. Figure 12 (b) shows $\delta q_{||}$ as a function of θ_n for the example of the profile in Figure 12 (a). The near and far SOL data are distinguished by different symbols. This clearly shows that $\delta q_{||}$ is strongly correlated with θ_n in the near SOL, which can also be seen as a measure of the toroidal distance from the limiter ridge. In other words the limiter geometry plays a significant role in the near SOL transport around the limiter. This is a strong indication that it is not upstream SOL physics but rather the local sink action of the limiter which is responsible for this enhanced heat flux. The fact that this funnel effect has not been observed in a divertor configuration [19] suggests that it is not only the grazing angle which is important but also the distance of the LCFS from the limiter surface.

Recently it has been shown numerically that solutions of the 2D non-linear heat diffusion equation exhibit strongly enhanced heat fluxes at the surface of a protruding object in the SOL of divertor plasmas [4]. This can be understood by noting that a sharp cold object attracts diffusive heat flux, similar to the enhanced local electrostatic field generated on the vicinity of a grounded electrical (both are governed by the Poisson equation). This analysis has been generalised to a 2D limiter geometry constructed to be analogous to the 3D JET inner limiter geometry (Figure 13 (a)). As illustated by Figure 13 (b), the finding is that the heat flux is again concentrated by the limiter, with a $(1/r_{mid})^{1/2}$ divergence in the effective $q_{||}$. The total heat flux reaches twice the extrapolated background heat flux at $r_{mid} \sim \lambda_{q,far}/8$ for a range of simulated $\lambda_{q,far}$ similarly to what is observed experimentally, and thus corresponds to a small fraction of the total heat flux. It arises because of the sharp edge at the centre (along the poloidal direction), which determines the contact point. The numerical calculations indicate that this enhanced heat flux could be eliminated by use of parabolically shaped limiter crown, which provides a cancelling divergence in ds/dr_{mid}, where s represents distance along the divertor surface.

Even if this model reproduces quantitatively the enhanced heat flux that we observe, there are two major assumptions that we are unlikely to full in our experimental conditions:

(i) The SOL must be in conduction-limited regime ignoring spatial density variation and assuming Spitzer-like parallel heat diffusivity: $\chi_{\perp} \propto T_e^{5/2}$ and Bohm-like perpendicular heat diffusivity: $\chi_{\perp} \propto T_e$

(ii) The temperature at the limiter face is assumed to be $T_e = 0$.

In other words, it requires a strong parallel temperature gradient, which is an unlikely condition for the SOL of JET limiter plasmas. Preliminary analysis of Langmuir probes (LP) embedded into the inner limiter show that the maximum electron temperature is at least of 28eV (when the RCP measures 38eV) at the closest position to the LCFS (for an ohmic plasma at $I_p = 2.5$MA). This model is therefore unlikely to explain our observation.

The alternative is to explore the funnel effect described in [8] but it requires some modications. There are two key assumptions in this model that do not apply for the JET case:

(i) The model is developed for a blunt-nose limiter, where magnetic field line are perfectly tangential to the limiter surface.

(ii) The model describes the particle flux, not the heat flux.

Current work is undertaken to adapt this model to JET conditions but this work goes beyond the scope of the present paper.

CONCLUSION

The important issue of first wall panel power loads to be expected on ITER during limiter start-up/ramp down has been addressed in dedicated experiments on JET in which SOL power profiles have been measured both by Langmuir probes in the main SOL and IR thermography of limiter tile surfaces. For high field side (inner wall) limiter configurations, which ITER expects to use widely for start-up, the IR data unequivocally show a region of high heat flux in the vicinity of the tangency point, where the JET tile design is such that there is reasonably sharp ridge in the centre of the tile, but at which conventional field line mapping assuming the usual exponential profile of parallel power ow in the main SOL finds low surface power densities. The JET reciprocating probe does indeed find such a profile, whose characteristic width is consistent with IR data mapped back along SOL field lines for radial distances a few mm outside the LCFS. This anomalous tangency point heat flux seen at the inner wall is not, however, found on low field side limiter tiles in outer limiter configurations, even though the tile design is similar to those on the inner wall. The enhanced inner wall feature may be a consequence of a particle funnelling effect reported in the past from other devices, or possibly as a result of diffusive attraction of the heat flux at the limiter ridge. Numerical calculations of this latter effect in simplified geometry yield results not inconsistent with the experimental observation. However, the assumptions in this model are unlikely to be fulfilled in the present experiments. These experiments demonstrate that conventional field line mapping of exponential SOL power profiles onto ITER inner wall limiter surfaces may not provide the correct surface power load distribution, but understanding of the physics driving the enhanced heat load is as yet insufficient to extrapolate the effect to ITER.

ACKNOWLEDGEMENT

This work, supported by the European Communities under the contract of Association between EURATOM and CCFE, was carried out within the framework of the European Fusion Development Agreement. The views and opinions expressed herein do not necessarily reflect those of the European Commission. This work was also part-funded by the RCUK Energy Programme under grant EP/I501045.

REFERENCES

[1]. R.A. Pitts, S. Carpentier, F. Escourbiac, T. Hirai, V. Komarov, A.S. Kukushkin, S. Lisgo, A. Loarte, M. Merola, R. Mitteau, A.R. Raray, M. Shimada, and P.C. Stangeby. Physics basis and deisgn of the ITER plasma-facing components. Journal of Nuclear Materials, **415**:S957–S964, 2011.

[2]. M. Firdaouss, V. Riccardo, V. Martin, G. Arnoflux, and JET-EFDA Contributors. Modelling of power deposition on the JET ITER-like wall using the code PFCFLFlux. Proc. in 20th PSI conference, Aachen, Germany, 2012.

[3]. R.J. Goldston. Downstream heat flux profile versus midplane T profile in tokamaks. Physics of plasmas, **17**:012503, 2010.

[4]. R.J. Goldston. When is it vald to assume that heat flux is parallel to B? Journal of Nuclear Materials, **415**:S566–S569, 2011.

[5]. G.F. Matthews, S.J. Fifieldings, G.M. McCracken, C.S. Pitcher, P.C. Stangeby, and M. Ulrickson. Investigation of the fluxes to a surface at grazing angles of incidence in the tokamak boundary. Plasma Physics and Controlled Fusion, **32**:1301–1320, 1990.

[6]. D. Guilhem, J. Hogan, T. Aniel, S. Boddeker, C. Grisolia, T. Hoang, G. Martin, B. Meslin, R. Mitteau, R. Reichle, and J.C. Vallet. Limiter heat load and consequences on impurity source and transport. Journal of Nuclear Materials, 2**66-269**:272–279, 1999.

[7]. C.H. Skinner, J.T. Hogan, J.N. Brooks, W. Blanchard, R.V. Budny, J. Hosea, D. Mueller, A. Nagy, and D.P. Stotler. Modeling of tritium retention in TFTR. Journal of Nuclear Materials, **266-269**(940–946), 1999.

[8]. P.C. Stangeby, C.S. Pitcher, and J.D. Fielder. The nature of plasma fluxes to surfaces nearly tangential to the magnetic field. Nuclear Fusion, **32**:2079{2089, 1992.

[9]. ITER Physics Expert Group on divertor. ITER physics basis, chapter 4: Power and particle control. Nuclear Fusion, **39**(12):2391–2469, 1999.

[10]. J. Gunn, R. Dejarnac, P. Devynck, N. Fedorczak, V. Fuchs, C. Gil, M. Kocan, M. Komm, M. Kubic, T. Lunt, P. Monier-Garbet, J.-Y. Pascal, and F. Saint-Laurent. Scrape-off layer power flux measurements in the Tore Supra tokamak. Proc. of 20th PSI conference, Aachen, Germany, 2012.

[11]. C. Silva, G. Arnoflux, S. Devaflux, M. Groth, J. Horacek, S. Marsen, G.F. Matthews, and JETEFDA Contributors. Comparison of scrape-off layer transport in inner and outer wall limited JET plasmas. Proc. of 20th PSI conference, Aachen, Germany, 2012.

[12]. E. Gauthier, H. Roche, E. Thomas, S. Droineau, B. Bertrand, J.B. Migozzi, W. Vliegenthart, L. Dague, P. Andrew, T. Tiscornia, and JET-EFDA Contributors. ITER-like wide angle infrared thermography and visible observation diagnostic using re ective optics. Fusion Engineering and Design, **82**:1335–1340, 2007.

[13]. V. Riccardo, P.J. Lomas, G.F. Matthews, I. Nunes, V. Thompson, and JET-EFDA Contributors. Design, manufacture an initial operation of the beryllium components of the JET ITER-like wall. Proc. of 27th symposium on fusion technology (SOFT), Liege, Belgium, 2012.

[14]. A. Herrmann, W. Junker, K. Gunther, S. Bosch, M. Kaufmann, J. Neuhauser, G. Pautasso, T. Richter, and R. Schneider. Energy flux to the ASDEX-Upgrade diverter plates determined by thermography and calorimetry. Plasma Physics and Controlled Fusion, **37**:17–29, 1995.

[15]. D. Rudakov, J.A. Boedo, R.A. Pitts, G.L. Jackson, C.J. Lasnier, A.W. Leonard, R.A. Moyer, P.C. Stangeby, G.R. Tynan, and J.G. Watkins. SOL width in limited versus diverted discharges in DIII-D. Journal of Nuclear Materials, **415**:S387–S390, 2011.

[16]. I. Nunes, V. Riccardo, P.J. Lomas, D. Alves, G. Arnoflux, S. Devaflux, T. Farley, M. Firdaouss, S. Jachmich, G.F. Matthews, C. Reflux, and JET-EFDA Contributors. Be tile power handling and main wall protection. Proc. in 24th IAEA Fusion Energy Conference, San Diego, USA, (FTP/2-1Rb), 2012.

[17]. J.P. Gunn, C. Boucher, M. Dionne, I. Duran, V. Fuchs, T. Loarer, I. Nanobashvili, R. Panek, J.-Y. Pascal, F. Saint-Laurent, J. Stöckel, T. Van Rompuy, R. Zagorski, J. Adamek, J. Bucalossi, R. Dejarnac, P. Devynck, P. Hertout an dM. Hron, G. Lebrun, P. Moreau, F. Rimini, A. Sarkissian, and G. Van Oost. Evidence for poloidally localized enhancement of radial transport in the scrape-off layer of the Tore Supra tokamak. Journal of Nuclear Materials, **363–365**:484–490, 2007.

[18]. S. Carpentier, Y. Corre, M. Chantant, R. Daviot, G. Dunand, J.-L. Gardarein, J. Gunn, M. Kocan, C. Le Niliot, R. Mitteau, V. Moncada, P. Monier-Garbet, B. Pegourie, C. Pocheau,

R. Reichle, F. Rigollet, F. Saint-Laurent, J.-M. Travere, and E. Tsitrone. Study of heat flux deposition on the limiter of the Tore Supra tokamak.Journal of Nuclear Materials, **390-391**:955–958, 2009.

[19]. G.F. Matthews, D.N. Hill, and M. Ali Mahdavi. Angular dependence of power in the DIII-D divertor. Nuclear Fusion, **31**:1383, 1991.

Method	C	α
TUN	21	−0.52
TUN + RFA	31	−0.46

Table 1: Fit parameters of the q dependence on the normalise heating power using Equation (7)

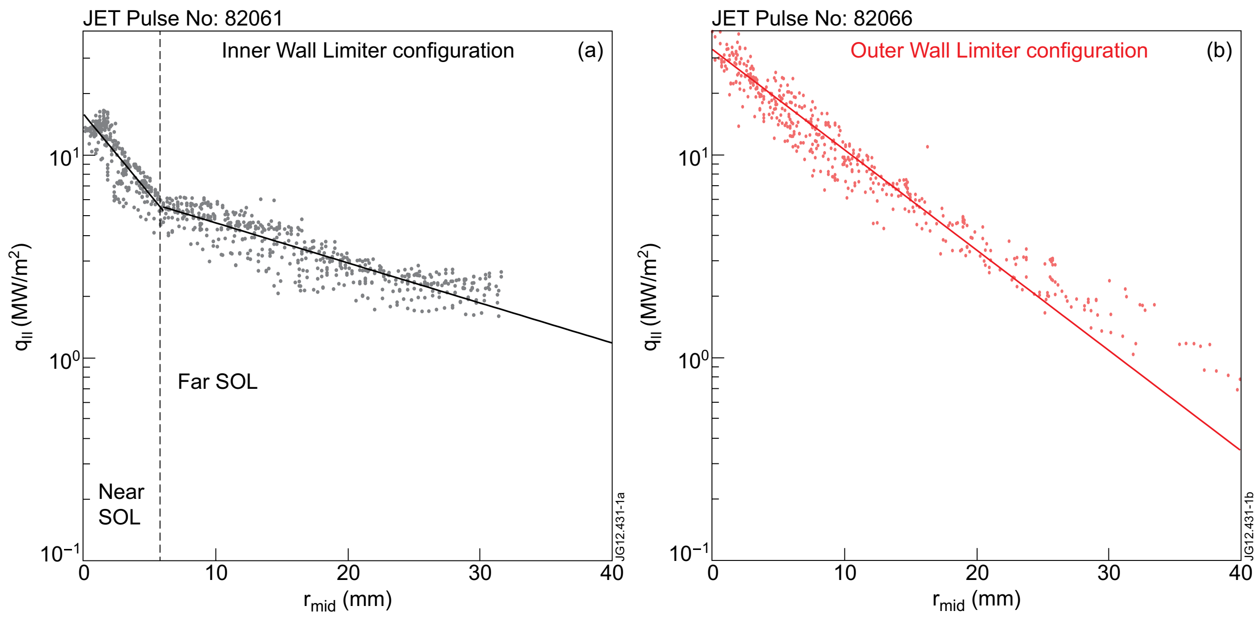

Figure 1: Inferred parallel heat flux profiles mapped to the omp, determined from the IR measurements at the limiter, of an IWL (a) and OWL (b) configuration. Note that the IR measurements correspond only to the interval $0 < r_{mid} < 40$ mm.

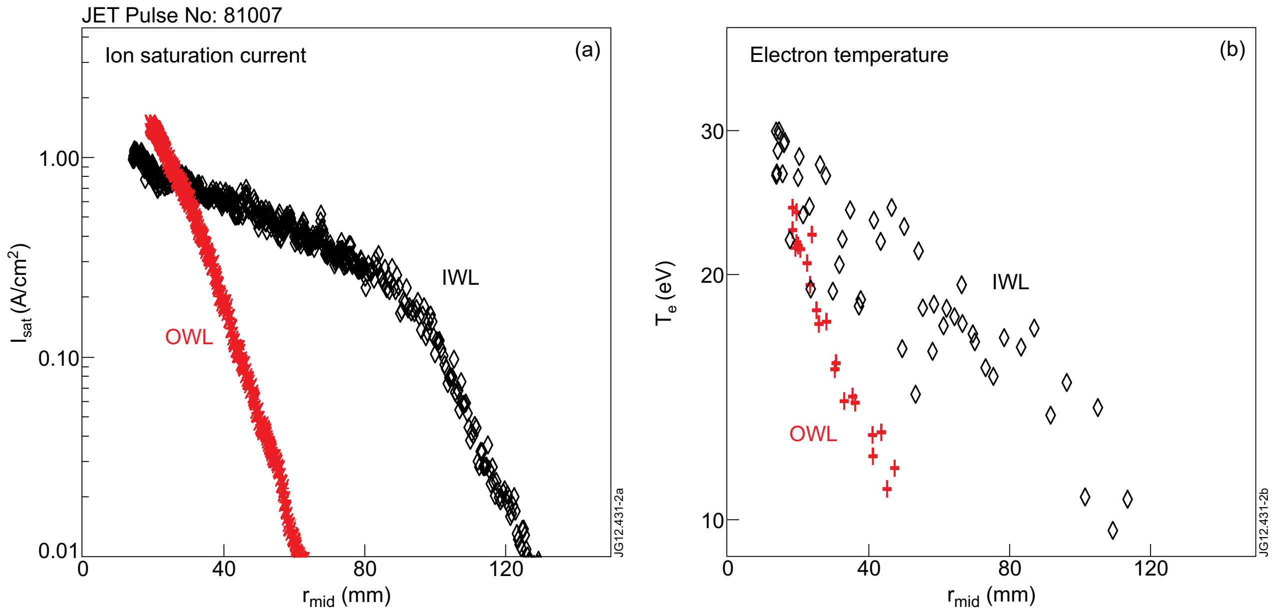

Figure 2: Ion saturation current (a) and electron temperature (b) proles of the SOL for an IWL and OWL configuration measured by the RCP. Note that the measurements cover an interval of 15 < r_{mid} < 130 mm.

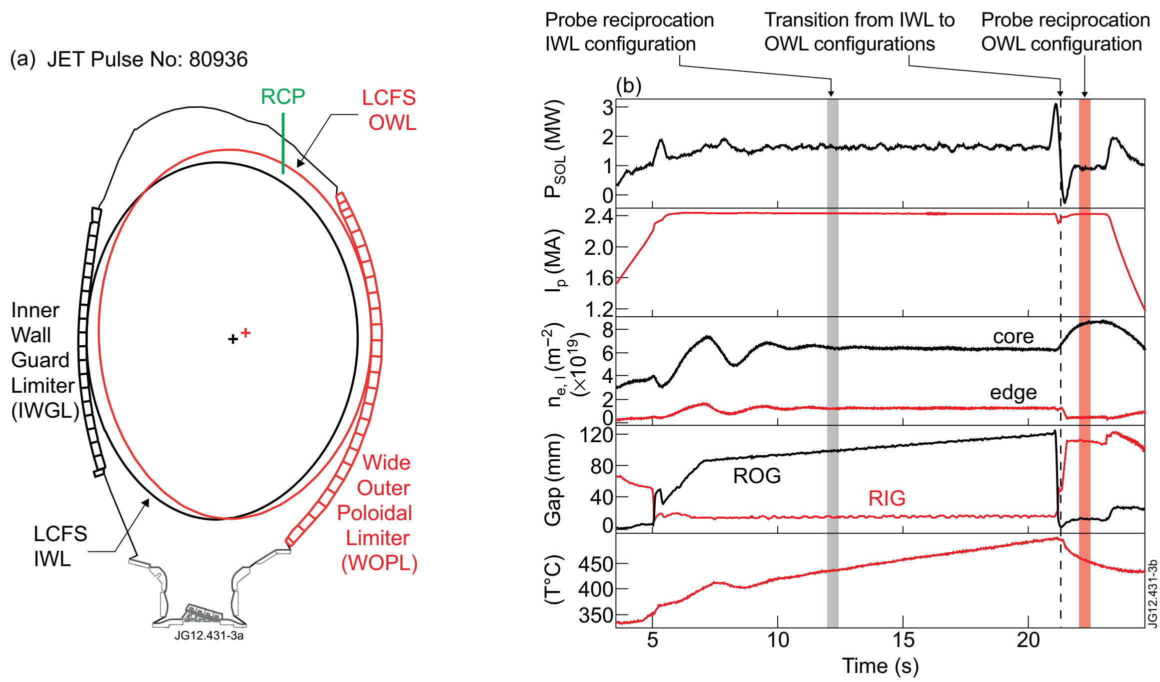

Figure 3: (a) Poloidal cross-section of JET with the key PFCs (IWG and WOPL) and the LCFS of the two magnetic equilibrium in IWL (black) and OWL (red) configurations. (b) Typical scenario with (from top to bottom) the power entering the SOL, P_{SOL}, the plasma current, I_p, the line integrated density, $n_{e,l}$, in the core and edge plasmas, the radial distance between the LCFS and the outer (ROG) or inner (RIG) wall at z = 0, and the maximum temperature measured by the IR camera, here at the IWGL.

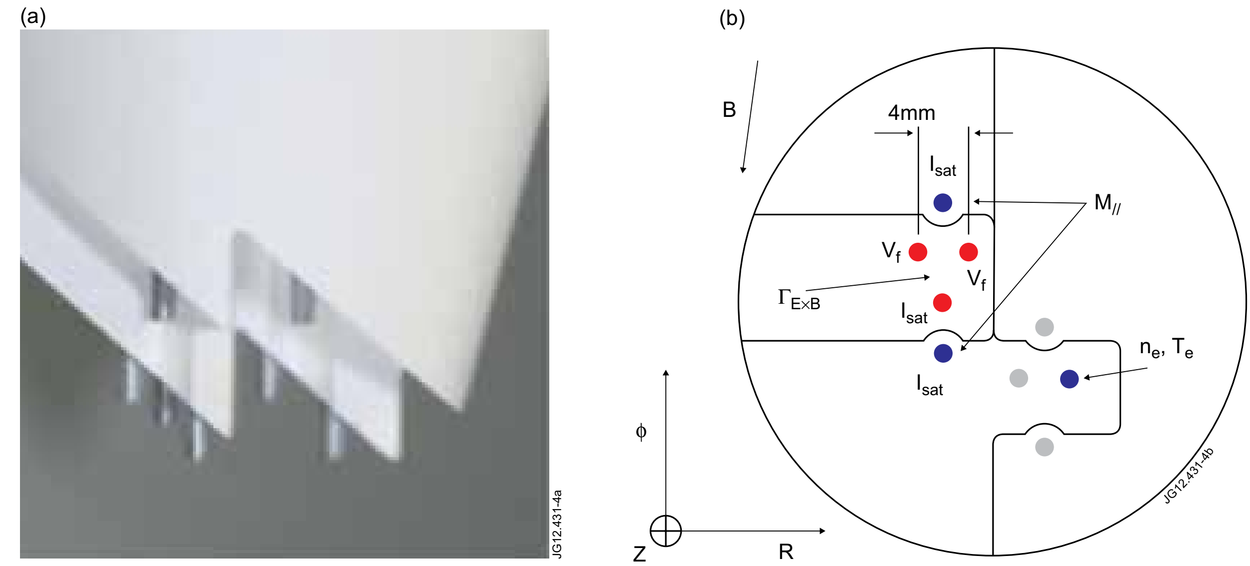

Figure 4: (a) Picture of the reciprocating probe head from the side (poloidal view). (b) Schematic representation of the probe pins distribution.

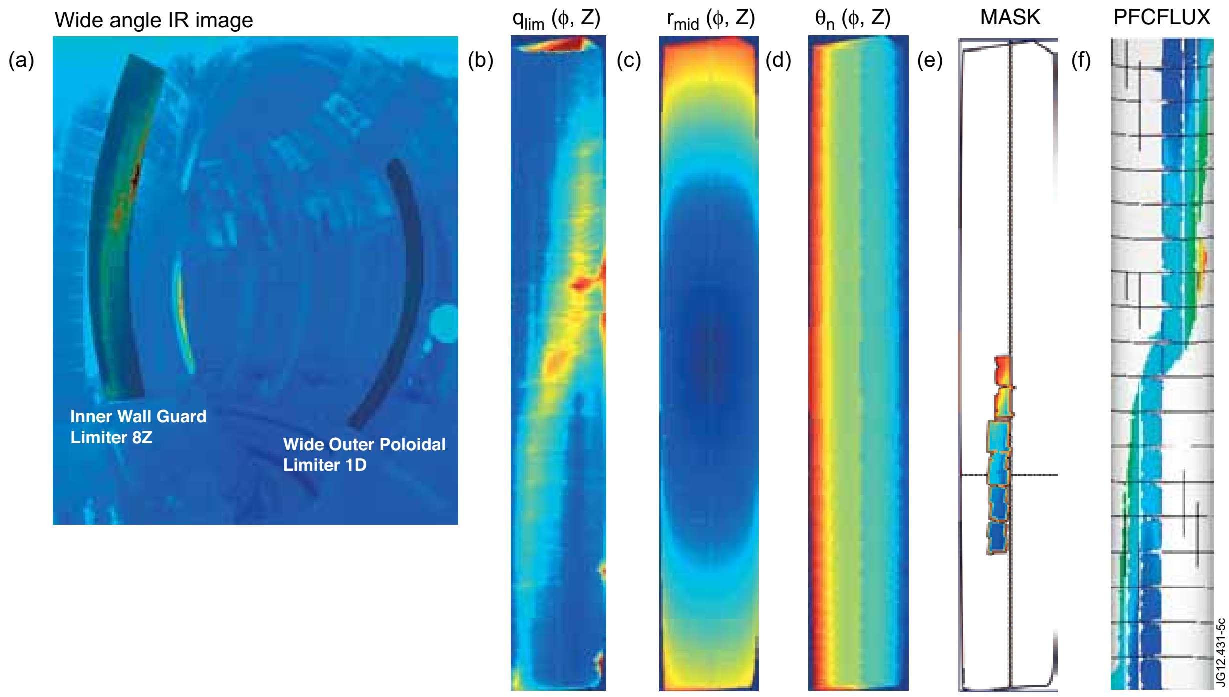

Figure 5: (a) Image taken by the IR wide angle view camera in JET, JET Pulse No: 80836. Dark red indicates the brightest (hottest) areas. Shaded areas delimit the key PFCs analysed in this paper. (b) map in the (z, ϕ) co-ordinate of the IR measured heat flux on the IWGL 8Z, (c) the corresponding omp radius, r_{mid}, (d) the eld line angle with respect to the normal vector to the PFC surface, θ_n, (e) mask (coloured region) of the pixels selected for the analysis, (f) the heat flux predicted by PFCFLUX (using λ_q = 30mm and P_{SOL} = 1.6MW)

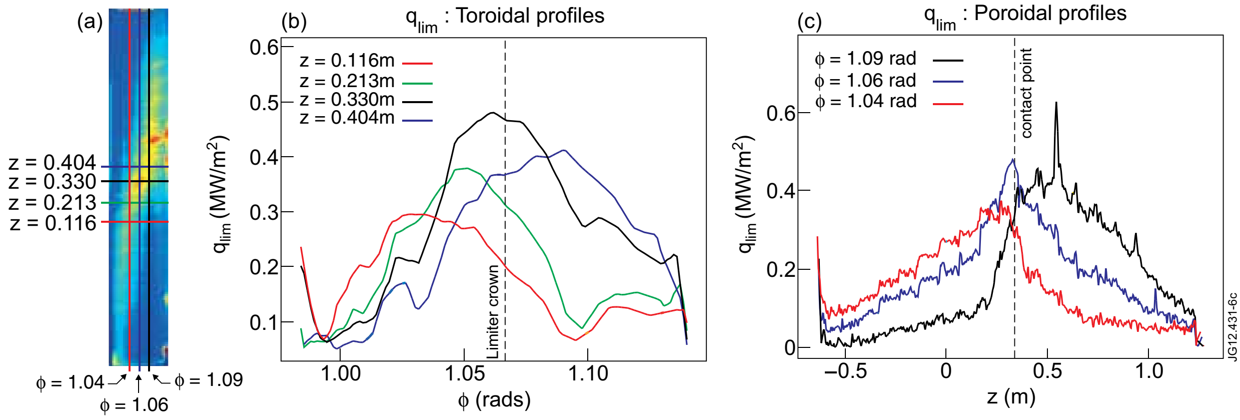

Figure 6: (a) Map of q_{lim} derived from the IR measurements for JET Pulse No: 80836. (b) Toroidal cuts of q_{lim} at 4 different vertical positions: z = 0.116; 0.213; 0.330 (plasma contact point) and 0.404m. (c) Poloidal cuts of q_{lim} at 3 different toroidal locations: ϕ = 1.04 (e-drift side), 1.06 (limiter apex) and 1.09 rads.

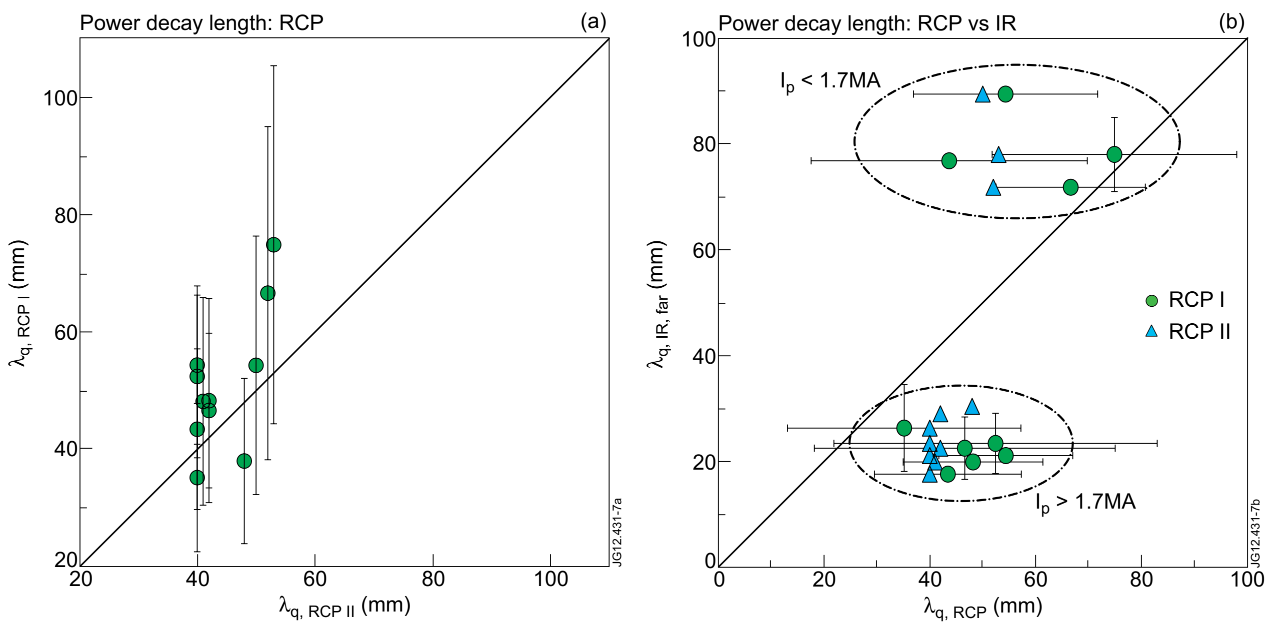

Figure 7: (a) Power decay length derived from the RCP measurements using method II as a function of that derived using method I. (b) Power decay length derived fromthe IR (far SOL) as a function of that derived from the RCP measurements.

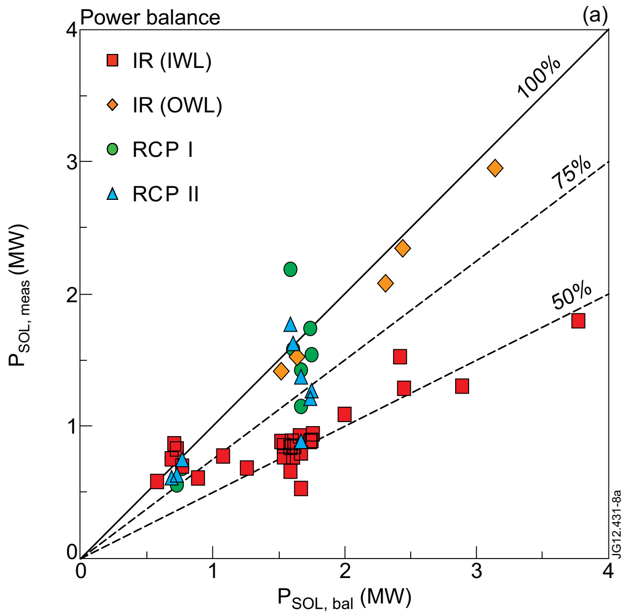

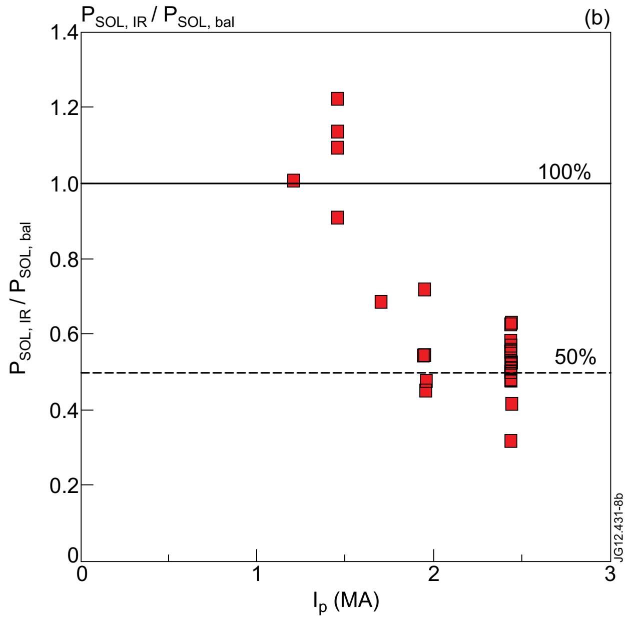

Figure 8: (a)$P_{SOL,meas}$ determined from IR and RCP inferred prole measurements (Equation (5) and Equation (4) respectively) as a function of $P_{SOL,bal}$ derived from the power balance (Equation (6)). (b) Ratio of power, $P_{SOL,IR}/P_{SOL,bal}$ for all the IR measurements in IWL configuration as a function of the plasma current, Ip.

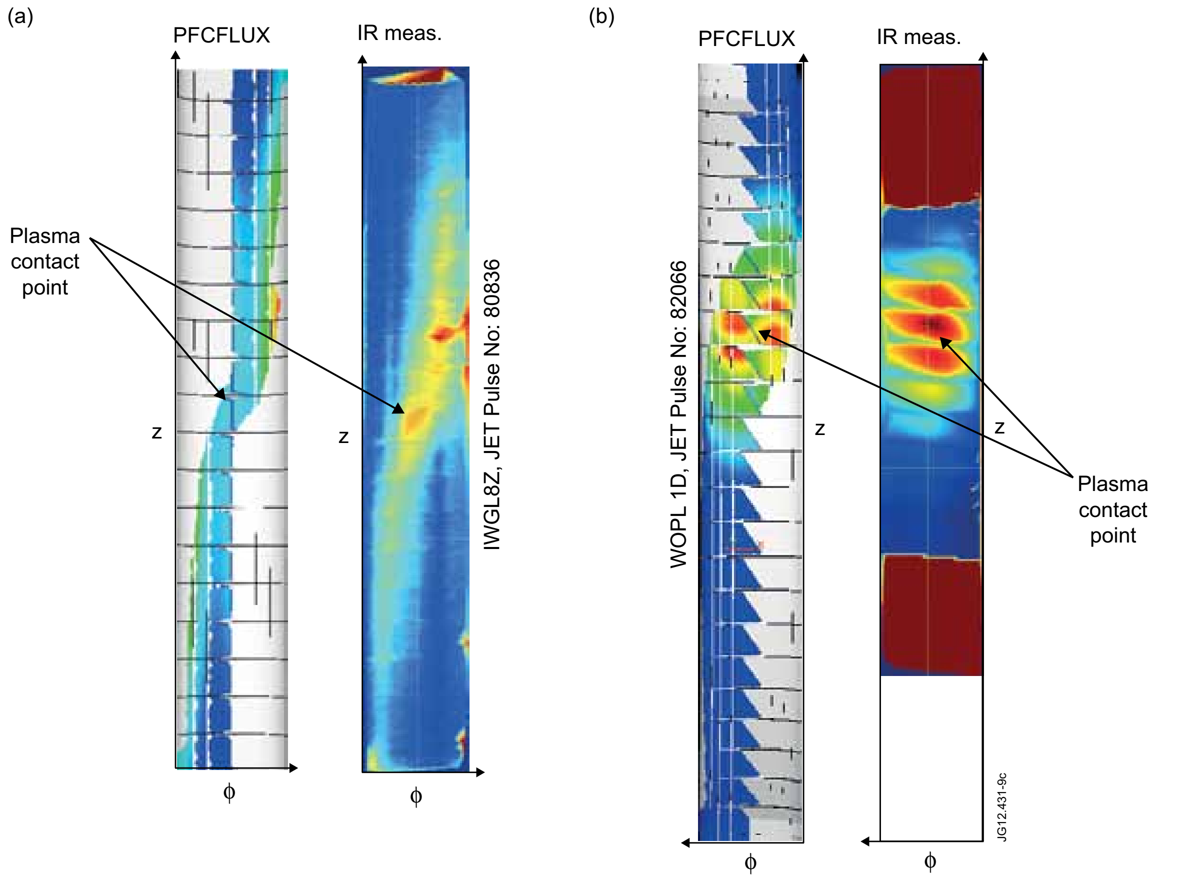

Figure 9: (a) and (b) heat load maps, $q_{lim}(\phi,z)$, on the IWGL and WOPL respectively, predicted by PFCFLUX and derived from the IR measurements.

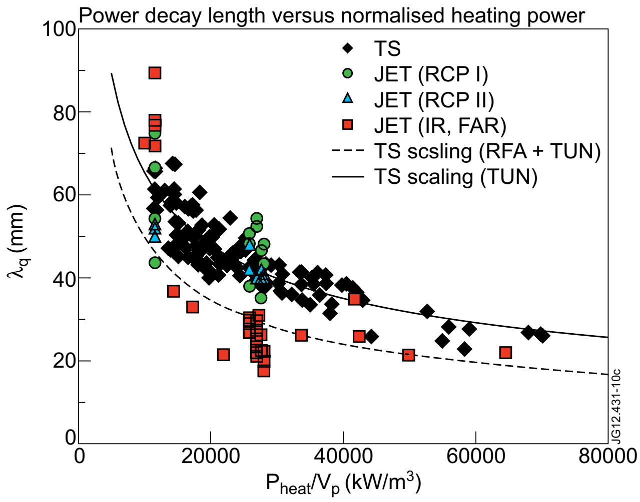

Figure 10: JET far SOL power decay length, measured with RCP (circles and triangles) and with IR (squares) compared with RCP measurements (diamonds) on TS, as a function of the heating power normalised to the plasma volume. The two scaling laws based on TS data are also shown.

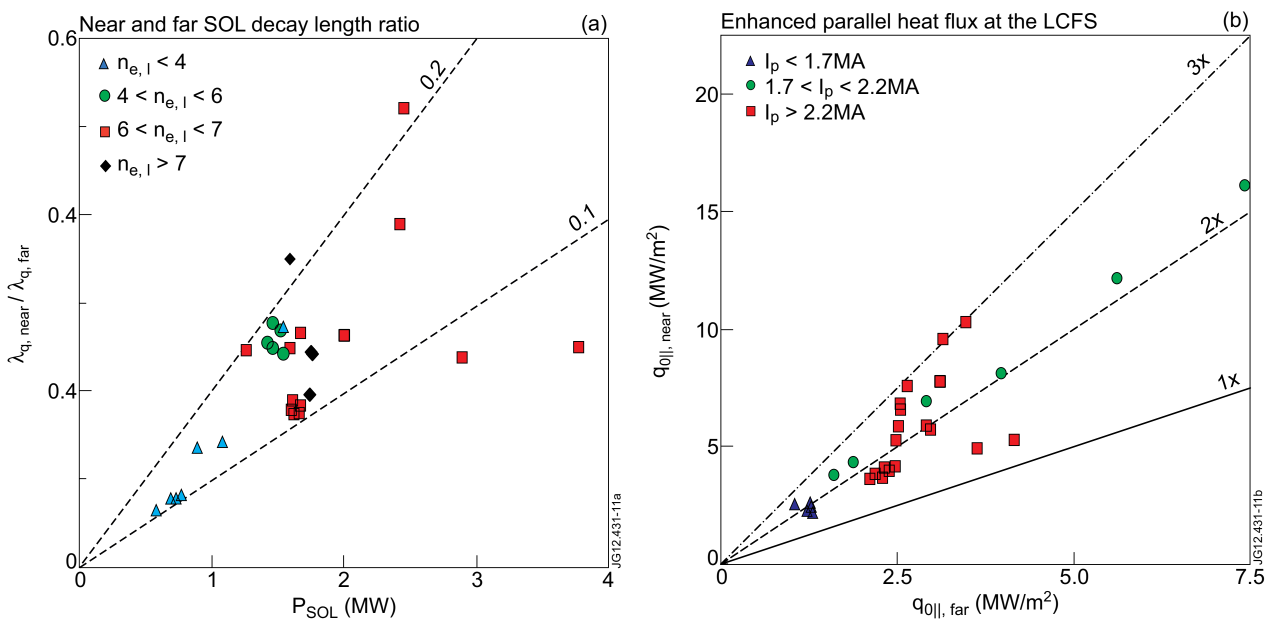

Figure 11: Characterisation of the enhanced $q_{||}$ profiles derived from the IR measurements using Equation (3) for the 30 JET pulses in IWL configurations. (a) Ratio of $\lambda_{q,near}/\lambda_{q,far}$ as a function of P_{SOL}. The symbols indicate different values of density (b) $q_{0||,near}$ as a function of $q_{0||,far}$. The symbols indicate dierent values of I_p.

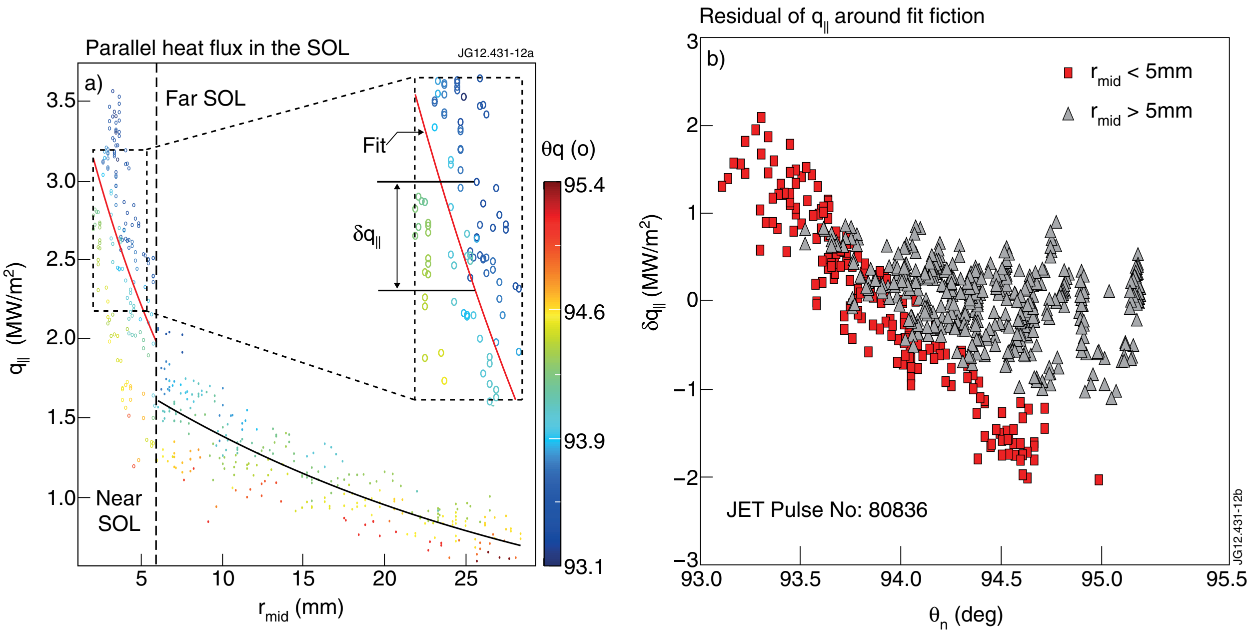

Figure 12: (a) Inferred parallel heat flux profile derived from the IR measurement on the IWGL 8Z as a function of rmid. The colour bar indicates the eld line angles on the limiter surface. Note that 93° < θ_n < 95°, which means that the field lines are never perfectly tangential to the limiter (θ_n = 90°). The data points are fitted with Equation (3). The definition of the residual, $q_{||}$ is show in the inset box (zoom into the near SOL part of the plot). (b) Residuals from the fit function as a function of the field line angle on the limiter surface, JET Pulse No: 80836.

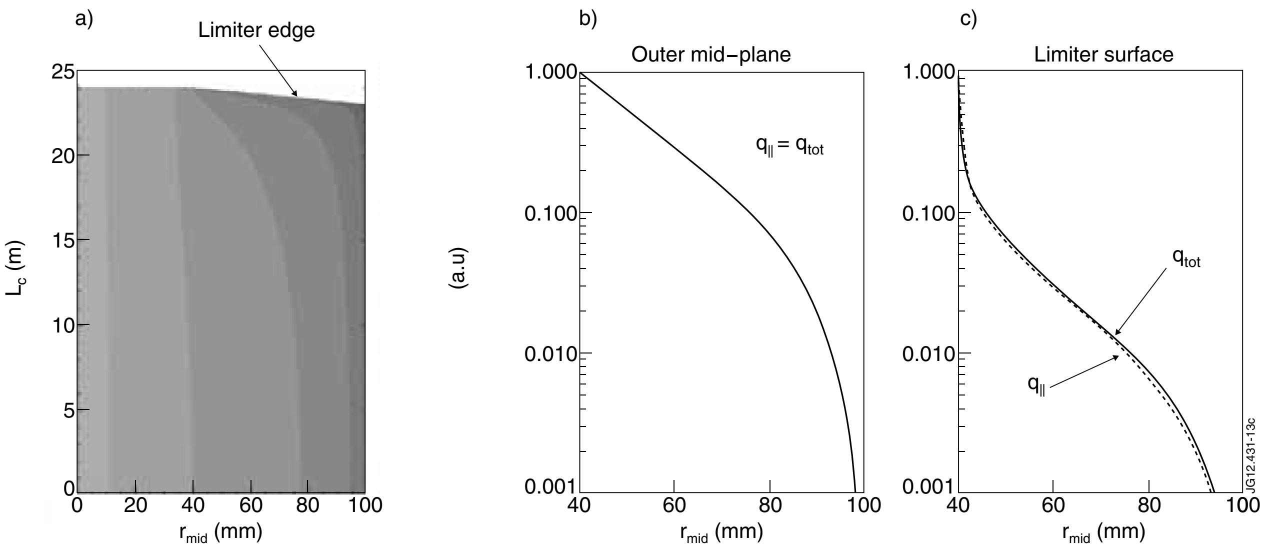

Figure 13: (a) Contour plot of the heat flux in the SOL as predicted by a solution of the 2D non-linear heat diffusion equation. L_c indicates the connection length between the limiter (L_c = 24m) and the omp (L_c = 0). (b) and (c) Total and parallel heat flux profiles at the omp and along the limiter respectively, as a function of r_{mid}.